A NEW APPROACH TO COMPUTATIONAL AEROELASTICITY

Oddvar O. Bendiksen *
Mechanical, Aerospace and Nuclear Engineering Department
University of California
Los Angeles, California

Abstract

In the present paper, we introduce a novel computational method for aeroelastic stability and structural response calculations. The entire fluid-structure system is treated as *one* continuum dynamics problem, by using a mixed Eulerian-Lagrangian formulation and switching from an Eulerian to a Lagrangian description at the fluid-structure boundary. This method has two important advantages. First, it effectively eliminates the phase integration errors associated with previous methods, where the fluid and the structure are integrated sequentially by different schemes. Second, it provides a systematic method for coupling finite element structural codes to finite volume fluid dynamics codes, in a manner that leads to highly vectorizable overall codes. The method is applied to transonic flutter calculations for wings and cascades, using simple finite element models. These results suggest that the method is capable of reproducing the energy exchange between the fluid and the structure with much less error that existing methods.

Nomenclature

a = speed of sound; also location of elastic axis

c = $2b$ = blade chord

e = total energy

f = body force

h = bending deflection, positive down

k = $\omega b/U$ = reduced frequency

K_h = typical section bending stiffness

K_α = typical section torsional stiffness

m = mass per unit span of blade

M = Mach number

p = pressure

q_i = generalized coordinates

r = position vector

r_α = nondimensional radius of gyration about EA

t = time

T = stress vector

T = kinetic energy

x_α = nondimensional CG-EA offset

u, v = velocities in x,y directions

U = mesh velocity vector

$\overline{U}$ = $U_\infty/b\omega_\alpha$

U = strain energy

U_∞ = freestream velocity at upstream infinity

α = angle of attack; also torsional deflection

β = $\sqrt{1-M^2}$

θ = stagger angle; also node rotation

μ = $m/\pi\rho b^2$ = mass ratio

ρ = air density

σ = interblade phase angle

ω = circular frequency, rad/s

ω_h = uncoupled frequency in bending

ω_α = uncoupled frequency in torsion

Superscripts and Subscripts

s = structure

f = fluid

∞ = conditions at upstream infinity

1.0 Introduction

Recent advances in supercomputer technology and computational methods are revolutionizing the fields of fluid and solid mechanics. Problems that only a few years ago were considered beyond the scope of theoretical calculations are now yielding to supercomputer simulations. The increased use of supercomputers to simulate the behavior of physical systems has also encouraged a reexamination of the existing *classical* approaches to certain problems. Indeed, shortcomings in computational procedures are often amplified in a parallel processing environment, because they typically prevent the generation of highly vectorized codes.

The difficulty in formulating efficient computational schemes for solving fluid-structure interaction problems arises from basic differences in the method of description and numerical schemes presently favored in fluid dynamics and in structural dynamics. In fluid dynamics, finite difference discretization procedures based on an Eulerian (spatial) description are firmly established, and it appears unlikely that finite element methods will displace finite difference methods in the near future. In structural dynamics, on the other hand, finite element methods based on a Lagrangian (material) description represent the state-of-the-art, and finite difference methods are considered archaic. Thus, when considering coupled fluid-structure (aeroelastic) systems, one is faced with interfacing

inherently incompatible numerical schemes, based on fundamentally different methods of description.

Given these difficulties, it is not surprising that existing computational techniques for fluid-structure interaction problems follow the *"classical approach"*, where the fluid and the structure are modeled separately and then coupled by specifying the kinematic boundary condition(s) at the fluid-structure boundary, e.g., Refs. 1-7. The kinetic (natural) boundary conditions provide forcing terms in the governing equations of motion for the structure. Since the boundary between the fluid and the structure still requires a Lagrangian method of description, the classical approach does not resolve all of the aforementioned problems. In fact, in order to impose the kinematic boundary conditions at time *t*, the location of the fluid-structure boundary must first be determined, and *this requires the solution of the entire system of equations for the structure.* But in order to solve the equations of motion for the structure, one also needs to know the generalized forces transmitted from the fluid to the structure (i.e., the kinetic boundary conditions), which are not available until the equations of motion for the fluid have been solved, and so on. Clearly, it is necessary to adopt some form of approximation procedure in this approach.

In the present paper, we take a new approach to the problem. Instead of adopting the classical computational strategy, we formulate the governing equations for both the fluid and the structure in integral conservation law form based on the same mixed Eulerian-Lagrangian description. At the fluid-structure boundary, we switch from an Eulerian (actually, a mixed Eulerian-Lagrangian) to a Lagrangian description, and from cartesian to generalized coordinates. The entire fluid-structure system is thus treated as one continuum dynamics problem, while still allowing for different discretizations in the two domains (if so desired). The same numerical integration algorithm can then be used throughout all elements in the field meshes covering the fluid-structure system.

In previous applications of mixed Eulerian-Lagrangian formulations, e.g. Refs. 8-9, the idea of a moving mesh was used either to simplify the treatment of the boundary nodes (since the boundary is Lagrangian), or to provide rezoning capability of the fluid mesh. A pure Lagrangian mesh is generally unsuited for the fluid domain, since mesh entanglement or excessive mesh distortion occurs if the fluid motion is sufficiently large. Because the governing equations resemble the Euler equations, they have also been referred to as Quasi-Eulerian, Arbitrary Lagrangian-Eulerian, or Referential. In computational aerodynamics, the moving mesh idea has found application in calculations of flows over wings and bodies [10,11]. However, in all of these earlier studies, the fluid-structure coupling was introduced in the classical manner.

The main objective of this paper is to demonstrate the technical feasibility of the proposed approach. First, we demonstrate how the integral form of the governing equations, applied to either a fluid or a solid element, can be used to couple finite difference Euler CFD codes to general purpose finite element codes for the structure. Second, we illustrate how the proposed computational strategy can be implemented to carry out aeroelastic calculations, and present a number of representative results.

Finally, we emphasize that the method presented in this paper applies to a wide class of fluid-structure problems in aeronautical, mechanical, civil, and marine engineering. Here, we focus on *aeroelastic* problems encountered in aircraft wings, helicopter rotors, and turbomachinery rotors.

2.0 Mixed Eulerian-Lagrangian Formulation

2.2 Governing Equations

The principles of classical mechanics can be stated in terms of three conservation laws: conservation of mass, conservation of momentum, and conservation of energy. In the present formulation, the last two are actually "balance laws" that specify how momentum and energy change under the influence of external forces.

Consider a finite region of a continuum, represented by a finite volume element (cell) of instantaneous volume V, as illustrated in Fig. 1. Let the instantaneous position of the surface of this cell be given by the equation

$$S(x,y,z,t) = 0 \qquad (2.1)$$

That is, a point P with coordinates (x,y,z) at time t that satisfy Eq. (2.1) lies on the surface S. The motion of the finite volume cell will be specified independently from the motion of the continuum; hence the cell does not constitute a material volume but rather an arbitrarily moving reference frame. The motion of the cell is specified by the velocity U of the boundary S:

$$\mathbf{U} = \dot{\mathbf{R}} = \dot{x}\mathbf{i} + \dot{y}\mathbf{j} + \dot{z}\mathbf{k} \qquad (2.2)$$

where $\mathbf{R}(x,y,z,t)$ is the position vector of a point $P(x,y,z,t)$ on the surface.

The conservation laws for mass, linear momentum, angular momentum, and energy for the volume V of the continuum enclosed by S can be stated in integral form as follows:

$$\frac{\partial}{\partial t}\int_V \rho \, dV + \int_S \rho \, (\mathbf{u} - \mathbf{U}) \cdot \mathbf{n} \, dS = 0 \qquad (2.3)$$

$$\frac{\partial}{\partial t}\int_V \rho \mathbf{u} \, dV + \int_S \rho \mathbf{u} \, (\mathbf{u} - \mathbf{U}) \cdot \mathbf{n} \, dS = \int_V \rho \mathbf{f} \, dV + \int_S \mathbf{T} \, dS \qquad (2.4)$$

$$\frac{\partial}{\partial t}\int_V \rho \mathbf{r} \times \mathbf{u}\, dV + \int_S \rho \mathbf{r} \times \mathbf{u}\,(\mathbf{u} - \mathbf{U}) \cdot \mathbf{n}\, dS = \qquad (2.5)$$

$$\int_V \rho \mathbf{r} \times \mathbf{f}\, dV + \int_S \mathbf{r} \times \mathbf{T}\, dS$$

$$\frac{\partial}{\partial t}\int_V \rho e\, dV + \int_S \rho e\,(\mathbf{u} - \mathbf{U}) \cdot \mathbf{n}\, dS = \qquad (2.6)$$

$$\int_V \rho \mathbf{u} \cdot \mathbf{f}\, dV + \int_S \mathbf{u} \cdot \mathbf{T}\, dS$$

The scalar variables ρ, p, and e are the density, pressure, and the specific total energy, respectively. The vectors $\mathbf{u}$, $\mathbf{T}$, and $\mathbf{f}$ are the velocity of the continuum, the stress vector on the surface, and the body force per unit mass, respectively. Here, $\mathbf{r}$ denotes the position vector from an arbitrary fixed point in the inertial reference system (x,y,z), and $\mathbf{n}$ denotes the outward unit normal to S.

The physical interpretation of Eqs. (2.3-6) is as follows. The first term on the left-hand side in each equation represents the change of the material quantity (mass, momentum, or energy) inside the cell, while the second term on the left-hand side represents the flux through the boundary S. The terms on the right-hand side represent source terms for momentum and energy. If we set $\mathbf{U} = \mathbf{0}$, we revert back to an Eulerian description. When $\mathbf{U} = \mathbf{u}$, we recover the Lagrangian form of the equations of motion. Finally, when $\mathbf{U} \neq \mathbf{u}$, we obtain the so-called mixed Eulerian-Lagrangian formulation. Note that from a mathematical standpoint, the equations resemble the Euler equations because of the presence of convective fluxes. Also note carefully that two reference frames are used in this formulation: an inertial system relative to which the velocities $\mathbf{u}$ and $\mathbf{U}$ and the position vectors are measured, and an intermediate frame defined by the finite volume cells relative to which the left-hand terms in Eqs. (2.3-6) are evaluated.

It is convenient to resolve the stress vector into normal and tangential components

$$\mathbf{T} = T_n^* \mathbf{n} + T_s^* \mathbf{s} = \sigma_{nn}\mathbf{n} + \sigma_{ns}\mathbf{s} \qquad (2.7)$$

where σ_{nn} and σ_{ns} are the normal and shear stresses at the surface. In the cartesian system, the components of the stress vector can be written in terms of the (cartesian) stress tensor σ_{ij} and the unit normal as

$$T_i^* = \sigma_{ij} n_j \qquad (2.8)$$

For an inviscid fluid, we set

$$\mathbf{T}_s = 0 \quad ; \quad \mathbf{T}_n = -p\mathbf{n} \qquad (2.9)$$

At this point, we specialize the equations to the two-dimensional case, which is implemented in the present paper. Using Eqs. (2.3-6), and observing that the unit vec-

tors normal and tangential to S can be written as

$$\mathbf{n} = \frac{dy}{ds}\mathbf{i} - \frac{dx}{ds}\mathbf{j} \qquad (2.10)$$

$$\mathbf{s} = \frac{dx}{ds}\mathbf{i} + \frac{dy}{ds}\mathbf{j} \qquad (2.11)$$

we obtain the following set of matrix equations:

$$\frac{\partial}{\partial t}\int_\Omega W dx dy + \int_{\partial\Omega}(F dy - G dx) = 0 \qquad (2.12)$$

where Ω is an element area with (moving) boundaries $\partial\Omega$ and

$$W = \left\{\begin{array}{c} \rho \\ \rho u \\ \rho v \\ \rho e \end{array}\right\} \qquad (2.13a)$$

$$F = \left\{\begin{array}{c} \rho(u-U) \\ \rho u(u-U) - \sigma_{nn} \\ \rho v(u-U) - \sigma_{ns} \\ \rho e(u-U) - \sigma_{nn}u - \sigma_{ns}v \end{array}\right\} \qquad (2.13b)$$

$$G = \left\{\begin{array}{c} \rho(v-V) \\ \rho u(v-V) + \sigma_{ns} \\ \rho v(v-V) - \sigma_{nn} \\ \rho e(v-V) + \sigma_{ns}u - \sigma_{nn}v \end{array}\right\} \qquad (2.13c)$$

and u,v and U,V are the cartesian components of $\mathbf{u}$ and $\mathbf{U}$, respectively. These equations can be applied to each finite volume cell of the continuum. For a cell occupied by an inviscid fluid, we set $\sigma_{nn} = -p$, $\sigma_{ns} = 0$, and use the perfect gas relation to eliminate p through the equation

$$p = \rho(\gamma - 1)[e - \frac{1}{2}\mathbf{u} \cdot \mathbf{u}] \qquad (2.14)$$

For a solid cell, such an elimination is not generally possible, because the internal energy depends on all six components of the stress tensor:

$$\rho e = U_0 + T_0 = \int_0^{\varepsilon_{ij}} \sigma_{ij} d\varepsilon_{ij} + \frac{1}{2}\rho(u^2 + v^2) \quad (2.15)$$

where U_0 and T_0 are the strain energy density and the kinetic energy per unit volume, respectively.

It should be noted that the conservation law for angular momentum leads to the conclusion that the stress tensor is symmetric, but does not contribute additional differential equations of motion in the small; that is, when

1714

applied to an infinitesimal volume. However, when a finite volume cell is considered, the conservation law for angular momentum in effect defines the motion of the material particles about the center of mass of the volume, whereas the conservation law for linear momentum defines the motion of the center of mass of the cell. For example, if we apply Eqs. (2.3-6) to a rigid-body cell, we expect to obtain six equations of motion: three governing the motion of the center of mass of the cell, and three governing the rotational motion of the body about the center of mass.

If one applies Eq. (2.12) to an infinitesimal volume and uses the divergence theorem, one obtains the differential equations of motion in cartesian coordinates. If applied to a "finite volume", Eq. (2.12) provides a convenient framework for obtaining space-discretized equations for the fluid domain. For the solid domain, one obtains Newton's equations in cartesian coordinates, which are seldom a convenient framework for studying structural dynamics. It is typically more efficient to use generalized coordinates and Lagrange's equations or Hamilton's principle to obtain the discretized equations of motion for a solid element (cell). However, the conservation laws expressed in integral form by Eq. (2.12) are still used as the basis for coupling fluid and solid cells.

2.3 Boundary Conditions

The kinematic boundary condition of tangent flow can be stated as

$$\frac{DB}{Dt} = 0 \text{, } or \quad \frac{\partial B}{\partial t} + \mathbf{u} \cdot \nabla B = 0 \qquad (2.16)$$

where $B(x,y,z,t)=0$ defines the instantaneous locus of the fluid-structure boundary. In the classical formulation, the kinematic boundary conditions are not enforced explicitly; that is, one does not enforce local force equilibrium between a fluid and a solid element at the boundary B, nor does one equate the energy flow or power at the common boundary.

In the present study, we enforce both kinematic and kinetic boundary conditions at the fluid-structure boundary. Since the mesh is attached to the structure and moves with it, we switch from an Eulerian to a Lagrangian formulation at the boundary. On the structural cell side, the velocity of the cell boundary coincides with the material velocity,

$$\mathbf{u}^s = \mathbf{U} \qquad (2.17)$$

On the fluid cell side, the fluid velocity normal to the boundary is equal to the velocity of the solid boundary normal to itself,

$$\mathbf{u}^f \cdot \mathbf{n} = \mathbf{u}^s \cdot \mathbf{n} = \mathbf{U} \cdot \mathbf{n} \qquad (2.18)$$

It is obvious from Eqs. (2.3-6) that enforcing Eq. (2.18) eliminates all convective fluxes across the edge of the solid element aligned with the boundary. The same must necessarily hold for the adjacent fluid element, because

$$\int_{\Omega} W(\mathbf{u} - \mathbf{U}) \cdot \mathbf{n} \, dS = \int_{\partial \Omega} W(u_n - U_n) dS \qquad (2.19)$$

obviously vanishes when the kinematic boundary condition, Eq. (2.18), is imposed. The reverse is also true; if the solution vector W is nonzero, then the vanishing of the convective fluxes through the boundary edge implies tangent flow, $u_n^f = U_n$. Thus the kinematic boundary condition can be imposed by zeroing out the convective fluxes at the fluid-structure boundary, leaving only the pressure terms in F and G.

In the far field, the boundary conditions must allow outgoing disturbances to pass with minimum reflection, and must also correctly describe the global behavior of the flow-field. At the upstream and downstream far-field boundaries we use nonreflecting boundary conditions of the type formulated by Hedstrom [12]. In the cascade calculations, phase-lagged periodic boundary conditions are applied at the boundaries of the reference channel.

3.0 Finite Volume - Finite Element Discretizations

3.1 Finite Volume Method

A practical and widely used discretization procedure for the Euler equations is the finite volume scheme introduced by Jameson, Schmidt, and Turkel [13]. This and other finite volume approximations based on the integral form of the equations of motion permit us to construct the solution in the physical plane, much in the same manner as is done in the finite element method. The method for constructing the discretized equations is different, however, and reduces essentially to central differencing in the space variables. The method is second-order accurate on a smooth mesh.

In this study, the computational domain is divided into quadrilateral cells, Fig. 1. If we apply the integral form of the conservation laws, Eqs. (2.12), to each fluid cell, we obtain a system of coupled ordinary differential equations of the form

$$\frac{d}{dt}(S_{ij}W_{ij}) + Q_{ij} - D_{ij} = 0 \qquad (2.20)$$

where S_{ij} is the cell area, W_{ij} is the vector of unknowns for cell (i,j), and Q_{ij} is the net flux out of the cells, contributed by the integral over $\partial \Omega$ in Eq. (2.12) and calculated as in Ref. 13. D_{ij} is a dissipative operator added to damp out numerical oscillations and to prevent decoupling of even and odd cells. The dissipative fluxes are constructed according to the idea of "adaptive dissipation" developed by Jameson and Baker [14]. Essentially, D_{ij} is a careful blend of second and fourth differences in the flow variables, or first and third order terms compared to the convective fluxes Q_{ij}. The first-order terms are only needed in the vicinity of shock waves, and are turned off in the smooth regions of flow, thus preserving the second-order accuracy of the scheme over most of the flow-field.

1715

The aeroelastic code is based on a cell-centered scheme for the fluid domain, where the flow variables are assumed constant over each cell and are stored at the cell centers. When calculating fluxes, the flow variables at a cell edge are taken as the average of the values in the cells on either side of the edge. Thus, although no formal interpolation functions are used as in the finite element procedure, the variables are interpolated in an approximately linear manner between cell centers.

If Eq. (2.12) is applied to each solid cell, a similar set of discretized equations would be obtained. Since the mesh is Lagrangian in the solid domain, and it is reasonable to treat the solid as incompressible in comparison to the fluid, the mass conservation equation can be dropped. The momentum equations reduce to Newton's second law for a particle:

$$\frac{d}{dt}(S\rho u)_{ij} - \int_{\partial\Omega} [\, i(\sigma_{nn}+\sigma_{ns})dy - j(\sigma_{nn}-\sigma_{ns})dx\,] = 0 \quad (2.21)$$

Unless we use a very fine mesh, the particle approximation is unacceptable, since it only defines the motion of the center of mass of the cell. We can augment Eq. (2.21) with the balance law for angular momentum, Eq. (2.5), and obtain a system that would be exact for a rigid element, and would model the rigid-body motion correctly for an elastic element. But much better tools exist, based on finite elements and Hamilton's principle.

3.2 Finite Element Method

For the solid elements, it is obviously advantageous to use a discretization procedure that is consistent with modern finite element theory. In particular, it is important that the finite element modeling of the structure be relatively general and not too dependent on the fluid modeling. This would allow direct use of existing finite element programs with their extensive finite element libraries, pre- and post-processors, and graphics capabilities. For these reasons, it is convenient to use generalized coordinates instead of the cartesian coordinates used in deriving the conservation laws, Eqs. (2.3-6). In addition, the formulation of the space-discretized equations is placed on a rigorous foundation, and Lagrange's equations or Hamilton's principle can be used to derive the equations of motion in the new coordinates. If the same underlying assumptions are made, then the conservation laws expressed by Eq. (2.12) will be satisfied for each element, and the interpolation errors inside each element are also minimized by the variational principle.

From a kinematic standpoint, the "closest" finite element to the cell-centered finite volume cell would be an element based on *linear* shape functions, that is, a constant-strain element. The simplest triangular element is of this type, but for a rectangular element the basic element is based on bilinear shape functions. Two or more constant-strain triangles can be joined to form a quadrilateral element that is "patch-wise" linear in the displace-

ments, as illustrated in Fig. 1b. In either case, if the elements are close to rectangular in shape and the mesh is smooth, the bilinear approximations in the FV and FE cells would be kinematically compatible, or as closely conforming as possible. Because two different approximation schemes are involved, it is not clear how the conformity requirement should be interpreted at the boundary between a solid and a fluid cell.

Instead of interpreting compatibility in purely kinematic terms, we propose that the concept be interpreted in terms of the basic conservation laws, and require that mass, momentum, and energy be conserved (or balanced) at the fluid-structure boundary, to within the discretization error of the overall scheme. If a variational principle exists for the coupled fluid-structure problem, this should lead to the same compatibility requirements as would be dictated by the variational principle. However, these compatibility conditions can be applied to problems where no variational principles are know.

In most cases of practical interest, different mesh densities would be called for in the fluid and solid domains. For maximum modeling flexibility, both the fluid and the solid element should be allowed interior nodes with respect to the other, as shown in Fig. 2. For example, in modeling thin compressor blades with plate elements, it would be reasonable to use a much coarser mesh for the structure, as suggested by Fig. 2a, especially in the leading and trailing edge regions where flow gradients may be high. But even in regions of smooth flow, more of constant-value FV cells would be required to approximate the cubic deflection and velocity fields of the FE plate elements at the fluid-structure boundary. This would also be the case in the modeling of typical aircraft wing structures, where beam and plate elements would be used extensively, as suggested in Fig. 3. We are then faced with the question of interpolating or transferring physical and kinematic variables between two different mesh densities at the fluid-structure boundary. Incidentally, this situation also arises in the implementation of multigrid solution algorithms for the fluid domain.

Consider a beam or plate element of unit width, as used in the present study; see Fig. 3b. The transverse displacement $w(\xi,t)$ inside a typical element is written in terms of the nodal coordinates q_k as follows:

$$w(\xi,t) = \sum_{k=1}^{4} N_k(\xi)q_k(t) \quad (2.22)$$

where the N_k's are cubic shape or interpolation functions. The generalized element coordinates q_k are calculated from the mesh coordinates x_{ij} and y_{ij} for the four mesh nodes defining the structural cell, using the kinematic constraint appropriate for this element. Because we are considering flexural deformations only, only four of the eight coordinates are linearly independent.

If a Galerkin discretization of the conservation laws or Largange's equations are applied to each finite element, discretized equations of a form similar to Eqs. (2.20) are obtained in the generalized element coordinates $\{q\}^{ij}$. In

the present paper, we use a *nodal* scheme for the structure, and write the discretized equations in terms of the nodal coordinates $\{q\}_{ij}$:

$$\frac{d}{dt}([m]_{ij}\{\dot{q}\}_{ij}) + \{Q^E\}_{ij} - \{Q^F\}_{ij} = 0 \qquad (2.23)$$

Here, the i,j subscripts refer to the (i,j) node, while elements are labeled with superscripts. For the wing structure in Fig. 3, the structural elements are at $j=1$, and we can drop the j-subscript and write

$$\{q\}_i^T = \{ w_i \quad \theta_i \} \qquad (2.24)$$

where w_i and θ_i are the transverse and rotational displacements at node $(i, 1)$, Fig. 3b. Here, $[m]_{ij}$ is the "nodal" mass matrix,

$$[m]_i = [m]_{22}^i + [m]_{11}^{i+1} \qquad (2.25)$$

in terms of the lumped *element* mass matrices for elements i and $i+1$, if the *ith* element matrix is partitioned into four 2x2 submatrices in the usual way. The generalized fluid pressure forces associated with the (i,j) element, $\{Q^F\}^{ij}$, are calculated by equating the corresponding virtual work expressions in the cartesian and the generalized coordinates. In terms of the fluid pressure on the lower and upper surface of the element, p_l and p_u,

$$Q_k^{Fij} = \int_0^{l_s} N_k(\xi)[p_l(\xi) - p_u(\xi)]d\xi \qquad (2.26)$$

In the nodal scheme, we set

$$Q_{1i}^F = Q_1^{F(i+1)} + Q_3^{Fi} \qquad (2.27a)$$

$$Q_{2i}^F = Q_2^{F(i+1)} + Q_4^{Fi} \qquad (2.27b)$$

The elastic forces $\{Q^E\}_{ij}$ forces are calculated in a similar manner, using the partitioned element stiffness matrices at the local element level:

$$\{Q^E\}_i = ([k]_{22}^i + [k]_{11}^{i+1})\{q\}_i \qquad (2.28)$$

$$+ [k]_{21}^i\{q\}_{i-1} + [k]_{12}^{i+1}\{q\}_{i+1}$$

That is, we do not need to assemble the structure and form global stiffness (or mass) matrices; only *local* assembly at the element (node) level is required, precisely as in the fluid domain. Another advantage arises from the fact that the solid mesh is *Lagrangian* and moves with the structure; this automatically accounts for geometrically nonlinear terms and the local linear stiffness matrices for the elements may be used, for sufficiently small elements.

In the present nodal scheme, Eqs. (2.23) have two degrees of freedom per node. However, since we need to know the actual nodal displacement vectors in order to move the mesh coordinates x_{ij}, y_{ij} in a Lagrangian fashion, we also need to perform another integration to get from $\{\dot{q}\}$ to $\{q\}$. This is all done simultaneously in the five-stage Runge-Kutta scheme, by writing the equations in

state-variable form by appending at each node the matrix identity

$$\frac{d}{dt}\{q\}_{ij} = \{\dot{q}\}_{ij} \qquad (2.29)$$

Finally, the energy equation for the structure is discretized and integrated as follows

$$\frac{d}{dt}(E_{tot}) = \dot{E}_{tot} = \sum_i \{\dot{q}\}_i^T \{Q^F\}_i \qquad (2.30)$$

where

$$E_{tot} = \sum_i (T_i + U_i) \qquad (2.31)$$

$$T_i + U_i = \frac{1}{2}\{\dot{q}\}_i^T[m]_i\{\dot{q}\}_i + \frac{1}{2}\{q\}_i^T[k]_i\{q\}_i \quad (2.32)$$

Note the obvious similarities between the structural equations, Eqs. (2.23), and the FV fluid equations, Eqs. (2.20). This allows us to use the same five-stage Runge-Kutta integration scheme for the entire fluid-structure domain and to treat the individual cells (i,j) the same, irrespective of whether they are solid or fluid cells. Of course, the variables calculated for solid and fluid cells differ, on account of our choice of generalized coordinates, but this is of no real concern to the computer.

4.0 Results and Discussion

4.1 Typical Section in Transonic Flow

A typical section isolated wing model has been implemented as indicated in Fig. 3. Here, a section of unit width in the spanwise direction is considered, in the spirit of the original ideas of Theodorsen and Garrick, but with two important differences. First, the section is allowed to have camber bending, and this "chordwise" flexibility is modeled by using plate-type finite elements of unit width; see Fig. 3b. Each element is allowed a hollow core, by specifying the effective structural skin thickness t_s for each element. Second, since the method of calculation is at the element level, an attempt is made to model the distributed restraining stiffness from the remainder of the wing on each element, by introducing bending and torsion springs at the element nodes.

The distributed bending and torsion stiffness coefficients are scaled proportional to the cube of the element thickness. In addition, the structural stiffness of the front and rear spars are superimposed, with numerical values tailored so as to place the elastic axis in the desired location, and to provide the desired values for the bending and torsion natural frequencies, ω_h and ω_α. The chordwise mass distribution is similarly tailored to get the sectional center of gravity in the desired location, by adding two tuning masses at the spar locations. Using this procedure, it is possible to construct our strip model for the wing structure such that, if it were constrained to two degrees of freedom (h and α) by letting the chordwise stiffness approach infinity, it precisely matches a giving

typical section model in all dynamical and structural properties. This careful construction of our model permits us to make direct comparisons between previous classical flutter calculations and calculations based on the present method, and also to assess the importance of camber bending in transonic wing flutter. It is recognized, of course, that in the case of low-aspect-ratio lifting surfaces, the present model cannot adequately account for the transverse (spanwise) effect and two-dimensional plate-type deformations must be modeled.

The NACA 64A006 typical section studied by Ashley [15] and also by Kousen and Bendiksen [5,6] was used as a starting point. In the notation used here, it has the following nondimensional parameters:

$$a = -0.2$$

$$x_\alpha = 0.2 \qquad (\chi_c = 0)$$

$$r_\alpha^2 = 0.29 \qquad (\rho_M^2 = 0.25)$$

$$\omega_h/\omega_\alpha = 0.3434 \quad (\omega_w/\omega_\theta = \sqrt{0.1})$$

To avoid confusion, the corresponding equivalent parameter values in Ashley's notation have been indicated in parenthesis. Table 4.1 summarizes the various aeroelastic cases calculated. Except as noted, we have used 5 finite elements in the chordwise direction; 3 elastic elements and two small rigid-body elements at the leading and trailing edges. An all aluminum structure was assumed, with $t_s/t = 0.05$, except as noted.

Table 4.1 Aeroelastic Cases: NACA 64A006 Wing

No.	M	$\overline{U}$	μ	Stability Behavior
1	0.87	2.00	10	Limit cycle
2	0.87	2.25	10	Limit cycle
3	0.92	2.02	10	Stable
4	0.92	2.20	10	Limit cycle
5	0.92	2.05	10	Limit cycle
6	0.92	2.50	50	Stable
7	0.92	3.00	50	Stable
8	0.92	5.00	50	Limit cycle
9	0.87	5.00	50	Explosive flutter

Figure 4 shows comparisons of the short- and long-term flutter behavior of the NACA 64A006 wing model for Case No. 1, as predicted using the present method of calculation and compared with predictions based on the classical approach, as implemented in Refs. 4-6. To provide meaningful comparisons, the fluid domain was modeled and solved in *exactly* the same manner as in Refs. 4-6, using the same mesh and the the same five-stage Runge-Kutta integration scheme. However, in the earlier method the structural equations were integrated *separately*, after the fluid equations had been advanced to the next stage within the multistage scheme. This necessitated an approximation for the lift and moment for the next time step, and a linear extrapolation was used in Refs. 4-6. In the present approach, no such approximation is necessary, since the entire domain of the continuum and all its cells are advanced simultaneously in time. That is, no distinction is made between solid and fluid cells during the actual time integration process.

From Fig. 4 it is evident, perhaps not surprisingly, that the aeroelastic response predicted by the two different methods of calculation do not stay the same for very long. It should be mentioned that the same steady solution was used as a starting point for the unsteady calculations, using exactly the same initial conditions ($h = 0.01\omega_\alpha b$). Part a) of the figure shows the transverse w-displacements at the leading edge (LE), midchord (MC), and the trailing edge (TE), during the first nine cycles of oscillation. Part b) shows plots of the local rotational amplitude θ at the same three locations (note that $\theta = -\alpha$ in the absence of camber bending). Part c) shows plots of the nondimensional total energy of the wing section (kinetic plus strain energy) vs. time, and the work done by the fluid pressure on all the finite elements making up the airfoil. Parts d), e) and f) show the aeroelastic behavior some 16 cycles later.

Since the structure has been modeled without damping, the difference between the total energy and the work should equal a constant, namely the initial energy of the structure (E0). By integrating the energy equation, we obtain an independent check on the accuracy of our method and the Runge-Kutta integration scheme. Note the excellent agreement between the initial energy and the difference (ETOT - WORK), represented by the diamonds for the present method, over the 34 cycles of oscillation covered in Fig. 4. These plots cover more than 20,000 time steps (each diamond represents 200-500 time steps). This attests to one of the main advantages of our method of calculation; namely, the fidelity by which the transfer of energy (and therefore also momentum) between the fluid and the structure is reproduced. Needless to say, this property is of utmost importance in aeroelastic calculations.

However, for the classical method of computation this (ETOT - WORK) difference, represented by square symbols, shows a systematic divergence away from the initial energy value E0. This error grows with increasing time, as is clear from the long-term plot, Fig. 4f. Also note that the long-term amplitudes differ by a considerable amount, roughly a factor of two, with the classical method

predicting larger amplitudes. According to earlier calculations, Fig. 3 of Ref. 6, a limit cycle is approached at roughly $t \approx 85$–90. It should be noted that the time scales differ by a factor of 5.673, since Ref. 6 nondimensionalized time with respect to ω_α, while here the following nondimensional time t is used:

$$t = \frac{STa_\infty}{2b} \qquad (4.1)$$

where T is the physical time, $2b = c$ is the airfoil chord, a_∞ is the speed of sound at infinity, and S is a scale factor introduced by the mesh routine. Here, $S = 0.15274$.

The relatively rapid growth of phase and frequency errors (or phase differences) between the two response predictions is also disconcerting and in need of an explanation. It seems plausible that the reason for the classical method predicting a higher flutter frequency, for example, is that it overestimates the energy flux from the fluid to the structure.

Figure 5 illustrates the stability behavior for the same wing section when the reduced velocity is increased to 2.25, while keeping the Mach number constant at 0.87. If Fig. 4b is compared to Fig. 4b in Ref. 5, we note that in this case, the present method predicts a *larger* limit cycle amplitude than does the classical method. Also, a definite structure emerges in the transverse and rotational displacement time traces, suggesting (perhaps) that a bifurcation to a periodic motion (limit cycle) with twice the original period has occurred. The energy traces for both total energy and work become very regular and display a periodic pattern containing *four* peaks. This fine structure did not show up in the "classical" calculations carried out in Ref. 5.

Case No. 3 was found to be stable by the present method of calculation, see Fig. 6, while the calculations by classical methods yielded a limit cycle, as indicated by the bifurcation diagram calculated in Ref. 5; see Fig. 7. Case No. 5 is very close to the linear flutter boundary according to the present method of calculation, as is evident from the slowly growing time traces in Fig. 8. When this case was calculated by the classical method, the corresponding flutter amplitudes were roughly five times as large at any given time t.

The mass ratio was then increased to $\mu = 50$, to get a representation of high-performance aircraft wings, and the structural thickness fraction was increased to $t_s/t = 0.5$. Using Fig. 9 of Ashley's study [15] of the same typical section model as a guide, calculations were made at various reduced velocities, in an attempt to locate the flutter boundary. Calculations at $\bar{U} = 2.5$ and 3.0 (Cases 6 and 7) were found to be stable (at $M = 0.92$) and are not plotted. Case No. 8, at $\bar{U} = 5.0$, yielded limit cycle flutter. This case was run both with five and with eight finite elements, Fig. 9, with no difference in the aeroelastic response predictions, to within plotting accuracy. The predictions using the classical computational method do, however, show significant differences, both in the flutter amplitudes as well as in the energy flow to the structure; see Fig. 10.

Note that in this case, in contrast to Case No. 1, the classical method *underpredicts* the response and the energy flow to the structure (i.e., the strength of the instability). Again, there is that troublesome discrepancy in the calculated work done by the fluid on the structure, which in this case is being systematically underestimated.

It is interesting to note that the flutter mode that eventually emerges and settles into a limit cycle has w and θ essentially in phase with each other at all chord locations. An examination of Fig. 8 for case 5 shows the same to be true in that case as well, but in Case No. 1, there is a small phase difference present between the local bending and torsional motions. Thus, although some of the data suggests that the shock-dominated limit cycle flutter that occurs may be a predominantly single-degree-of freedom phenomenon, further investigation of this point is called for.

Finally, Fig. 11 illustrates the dramatic sensitivity of this wing model to Mach number. Here, $\bar{U}$ is the same as in the previous case, but the Mach number has been decreased from 0.92 to 0.87. Explosive flutter results, and there is no evidence of limit cycles at realizable amplitudes; in fact, the twist amplitudes reached values of the order of 20 deg within the first two cycles of oscillation. Also note that w and θ are not in phase, and that this phase is largest at the leading edge and decreases towards the trailing edge, suggesting the presence of a traveling wave.

The results from these and other calculations seem to indicate that the aeroelastic response in the transonic region is quite sensitive to camber bending, presumably because of the sensitivity of the mixed subsonic-supersonic flow-field to small changes in the airfoil boundary condition in the *supersonic* region. However, the actual magnitude of the camber bending was always found to be relatively small in the wing calculations presented here, typically of the order of 2% of θ, or less than 0.2 deg.

4.2 Cascaded Airfoils; Wing in Wind Tunnel

It is well-known that the (2D) case of a wing oscillating in a wind tunnel is equivalent to an unstaggered cascade oscillating with an interblade phase angle of 180 degrees. If the tunnel height is h and the static position of the airfoil is at $h/2$, then the equivalent cascade would have a blade-to-chord spacing $s/c = h$. Linear theory predicts that the critical interblade phase angle for flutter for an unstaggered cascade is 180 deg; that is, adjacent blades are in anti-phase motion with respect to each other.

Here, the blades are modeled as thin isotropic plates of unit width in the spanwise direction, with typical section stiffness parameters except in the chordwise direction. The chordwise flexibility is modeled with plate-type finite elements, is done in the wing model. The structural model has been implemented as indicated in Fig. 3; that is, with the solid element free to have interior nodes with respect to the fluid element.

Although we have successfully used a one-to-one correspondence in test calculations, i.e., by simply extend-

ing the fluid mesh through the blade, this is not optimal for two reasons. First, since the fluid mesh requires small cell sizes in the leading and trailing edge regions, the finite elements would also be concentrated in these regions. Second, the extremely small structural elements that would result in the relatively thick leading edge region would severely limit the allowable time step in the explicit time integration of the aeroelastic equations. For numerical stability reasons, the maximum time step is limited by the Courant-Friedrichs-Lewy (CFL) condition, which implies that the maximum time step is inversely proportional to the highest characteristic wave speed in the element, and proportional to the representative length of the element.

The blades were solid titanium blades, of varying typical section stiffness in bending and torsion, nondimensionalized as follows:

$$\kappa_b = \frac{12c^3 K_b}{E t^3} \quad ; \quad \kappa_t = \frac{12c K_t}{E t^3} \quad (3.2)$$

Table 4.2 summarizes the cases discussed in the present paper.

Table 4.2 Aeroelastic Cases: Cascade

No.	M	κ_b	κ_t	Blade
1	0.825	4	*	NACA 006
2	0.850	3	1	NACA 003
3	0.850	3	1	NACA 002

* κ_t arising from distributed κ_b

An example of "classical" flutter behavior is shown in Fig. 12, representing the first case in Table 4.2. In this case, the sectional stiffness is modeled by distributing the "bending springs" over the chord, at the finite element nodes. This results in a relatively low torsional stiffness for the section, and flutter occurs in a predominantly torsional mode. Closer examination of the flutter mode reveals the presence of a bending component, which is not in phase with the torsional component. The chordwise bending modes, however, are not excited, although there is a small amount of camber bending in the flutter mode.

Figure 13 shows the results of aeroelastic calculations for Case No. 2, where the bending and torsion springs have been attached at the node at roughly 42% of chord. The time traces at $M = 0.85$ indicate a subcritical response over the first few cycles, as is evident by the fluid doing negative work and the total energy of the structure decreasing until t is about 5, after which the mean energy and work per cycle start increasing. At roughly $t = 10$, the work trace crosses zero and keeps on climbing, indicating that flutter has occurred. In this example, the camber bending is quite significant, as evident by the much larger

rotational (θ) amplitude at the trailing edge than at the midchord of the blade. The presence of the chordwise mode(s) is also evident in the time traces of the w-displacements, Fig. 13a.

Decreasing the blade thickness further from 3% to 2% of chord would be expected to further amplify the effect of chordwise bending on the flutter behavior of the blades. Figure 14 illustrates the gradual emergence of the chordwise bending mode in the flutter time traces for Case No. 3; see, in particular, the behavior of the θ displacement at the trailing edge vs. times, and the strong oscillations in the total energy and work traces. In this example, the trailing edge region develops large-angle rotational displacements wherein it moves almost like a trailing edge flap. It is believed that the taper of the blade in this region helps localize and amplify the motion in the thin trailing edge region.

5.0 Conclusions

The main conclusions can be summarized as follows:

1. The proposed method of calculating aeroelastic response has a number of important advantages over existing methods, and is capable of handling realistic structures modeled by finite elements. This modeling can be done at the *element* level.

2. Because there is no assembly of mass and stiffness matrices into global (system) matrices, there is no need to introduce special procedures for dealing with sparse matrices. Because of the Lagrangian mesh, *geometrically nonlinear* problems can be treated without the use of geometric stiffness matrices.

3. The excellent accuracy by which it reproduces the energy exchange between the structure and the fluid makes the method especially suited for large-scale (supercomputer) simulations.

4. Results from the sample calculations suggest that camber bending can play an important role in the transonic flutter problem, possibly because the mixed subsonic-supersonic flow field is very sensitive to the airfoil boundary condition in the supersonic region of the flow.

5. Calculations made on cascades with solid titanium blades indicate that camber bending can reach significant amplitudes during transonic flutter of thin compressor blades.

References

[1] Bisplinghoff, R. L. and Ashley, H., *Principles of Aeroelasticity*, John Wiley and Sons, New York, 1962.

[2] Edwards, J. W., et al., "Time-Marching Transonic Flutter Solutions Including Angle-of-Attack Effects," *Journal of Aircraft*, Vol. 20, Nov. 1983, pp. 899-906.

[3] Yang, T. Y., Guruswamy, P., and Striz, A. G., "Application of Transonic Codes to Flutter Analysis of Conventional and Supercritical Airfoils," *Journal of Aircraft*, Vol. 19, March 1982, pp. 211-220.

[4] Bendiksen, O. O. and Kousen, K. A., "Transonic Flutter Analysis Using the Euler Equations," AIAA Paper 87-0911-CP, April 1987.

[5] Kousen, K. A. and Bendiksen, O. O., "Nonlinear Aspect of the Transonic Aeroelastic Stability Problem," *Proc. AIAA/ASME/ASCE/AHS 29th SDM Conf., Williamsburg, Virginia, April 18-20, 1988, pp. 760-769.*

[6] Kousen, K. A. and Bendiksen, O. O., "Limit Cycle Phenomena in Computational Transonic Aeroelasticity," *Proc. AIAA/ASME/ASCE/AHS 30th SDM Conf., Mobile, AL, April 3-5, 1989, pp. 230-240.*

[7] Batina, J. T., Bennett, R. M., Seidel, D. A., Cunningham, H. J., and Bland, S. R, "Recent Advances in Transonic Computational Aeroelasticity," *NASA Technical Memorandum 100663*, Sept. 1988.

[8] Hirt, C. W., Amsden, A. A., and Cook, J. L., "An Arbitrary Lagrangian-Eulerian Method for all Flow Speeds," *Journal of Computational Physics*, Vol. 14, No. 3, 1974, pp. 227-254.

[9] Donea, J., Guiliani, S., and Halleux, J. P., "An Arbitrary Lagrangian-Eulerian Finite Element Method for Transient Dynamic Fluid-Structure Interactions," *Computer Methods in Applied Mechanics and Engineering*, Vol. 33, 1982, pp. 689-723.

[10] Steger, J. L., "Implicit Finite-Difference Simulation of Flow about Arbitrary Two-Dimensional Geometries," *AIAA Journal*, Vol. 16, July 1978, pp. 679-686.

[11] Jameson, A. and Venkatakrishnan, V., "Transonic Flows About Oscillating Airfoils Using the Euler Equations," AIAA Paper 85-1514-CP, July 1985.

[12] Hedstrom, G. W., "Nonreflecting Boundary Conditions for Hyperbolic Systems," *Journal of Computational Physics*, Vol. 30, 1979, pp. 222-237.

[13] Jameson, A., Schmidt, W., and Turkel, E., "Numerical Solutions of the Euler Equations by Finite Volume Methods Using Runge-Kutta Time Stepping Schemes," AIAA Paper 81-1259, 1981.

[14] Jameson, A. and Baker, T. J., "Solution of the Euler Equations for Complex Configurations," *Proc. AIAA 6th Computational Fluid Dynamics Conference*, Danvers, MA, 1983, pp. 293-302.

[15] Ashley, H., "Role of Shocks in the 'Sub-Transonic' Flutter Phenomenon," *Journal of Aircraft*, Vol. 17, March 1980, pp. 187-197.
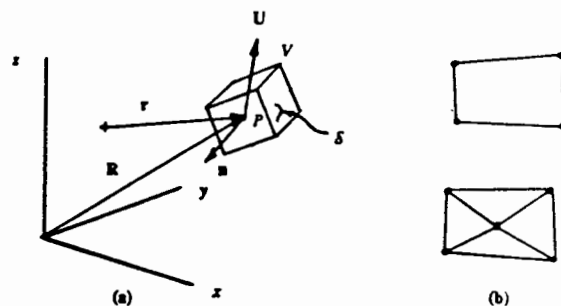
Fig. 1 Typical elements

(a)   (b)
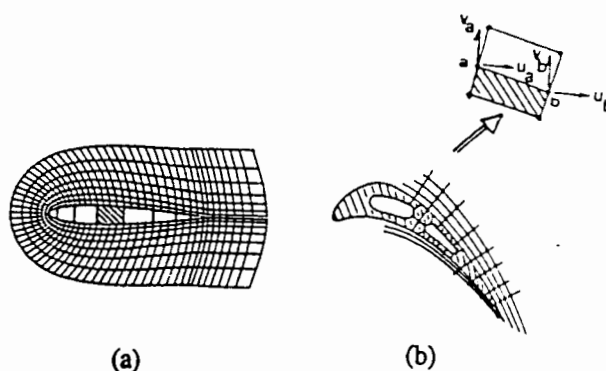
Fig. 2 Fluid-structure mesh, and examples of interior nodes
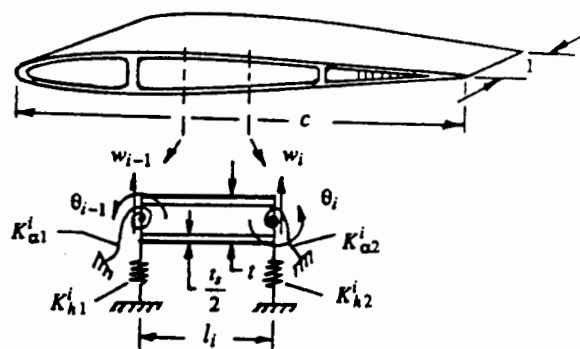
Fig. 3 a)Typical section wing structure with camber bending; b) basic finite element
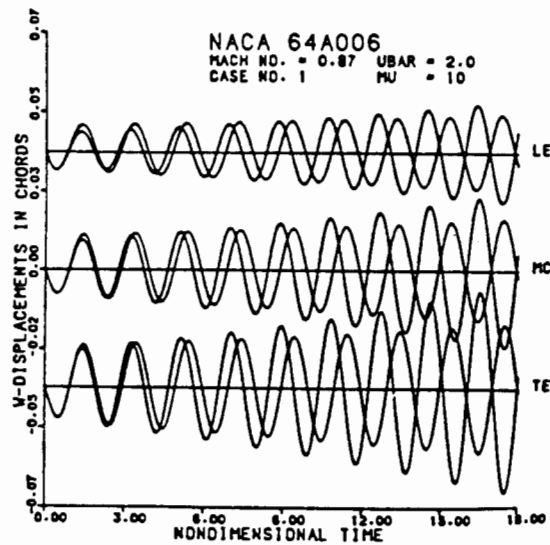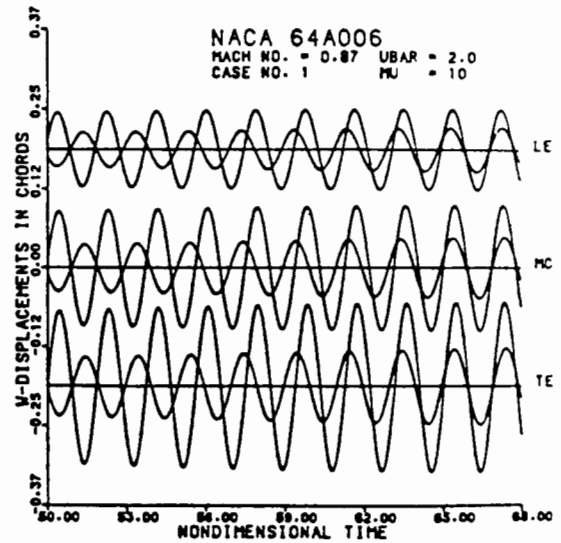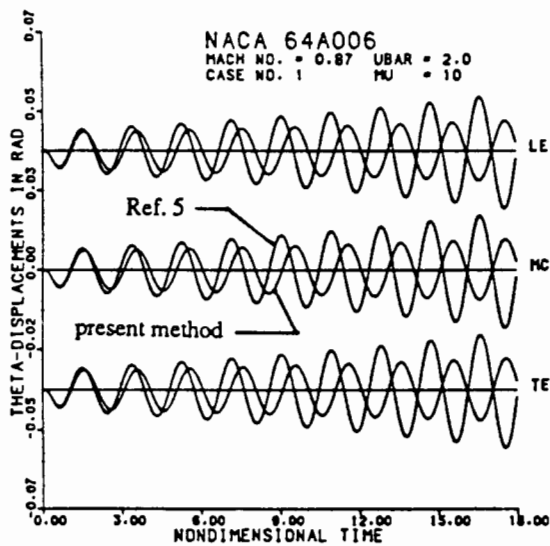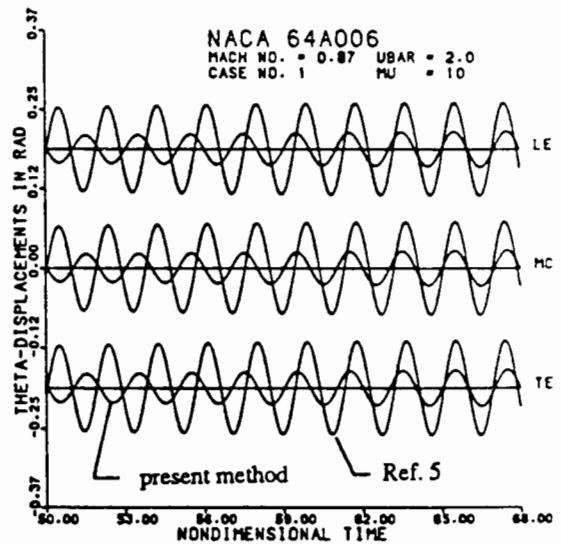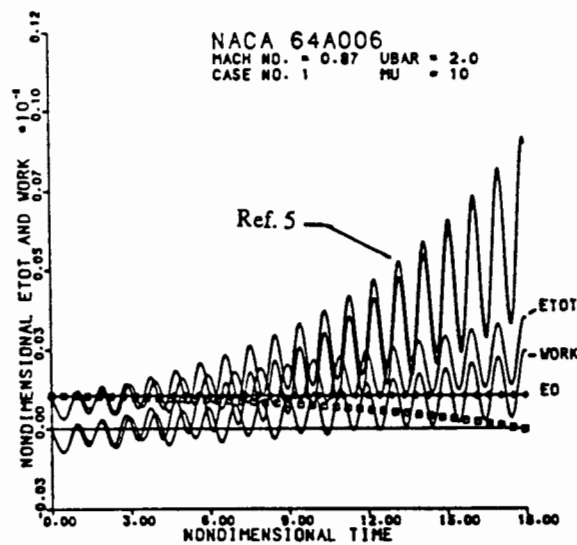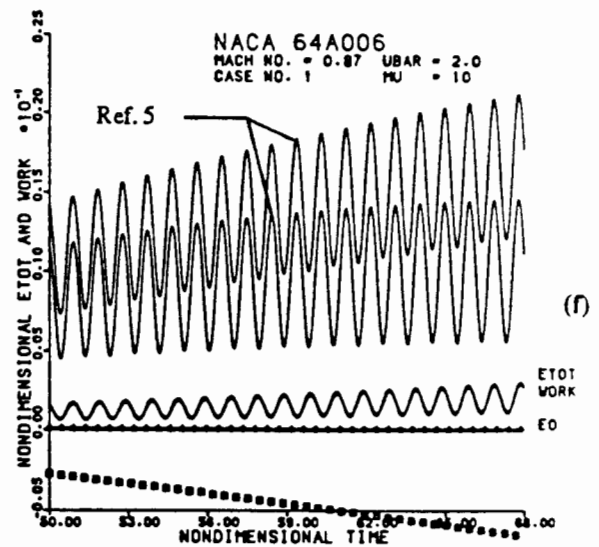
Fig. 4 Comparison of aeroelastic response of NACA 64A006 wing model for Case No. 1, as predicted by present approach and compared to classical approach (Ref. 5)
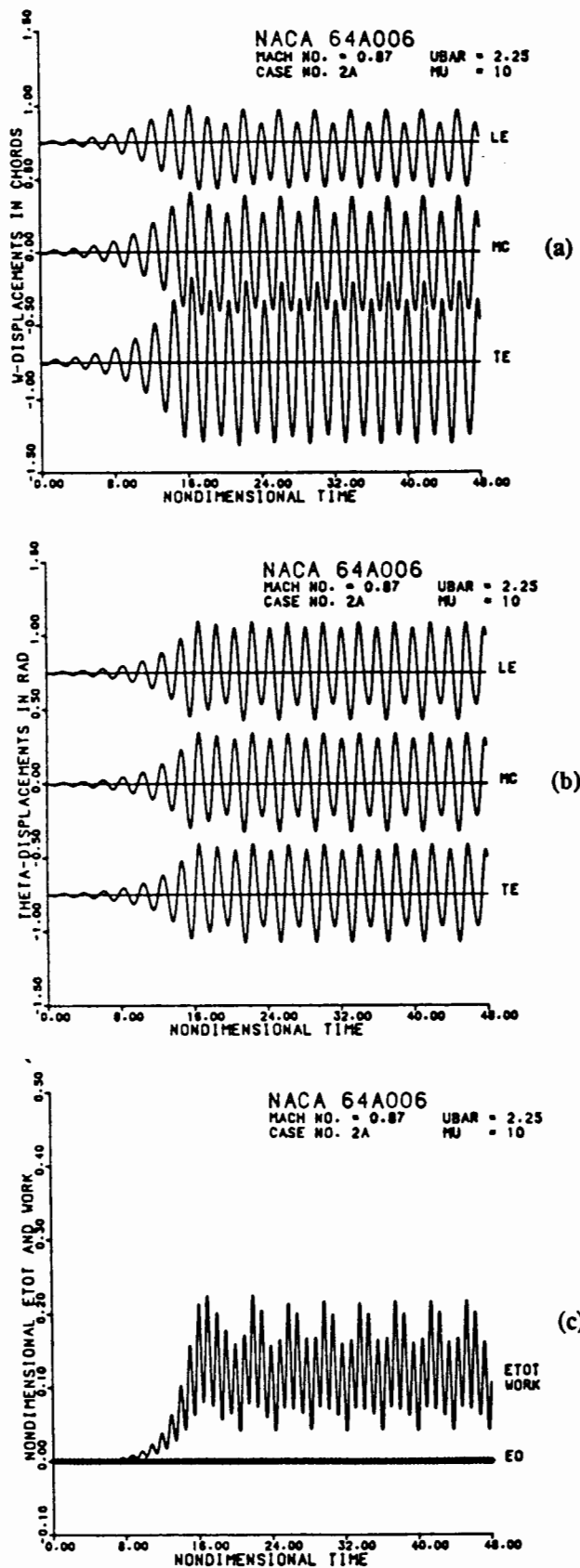
Fig. 5 Aeroelastic response of NACA 64A006 wing for Case No. 2, as calculated by present method
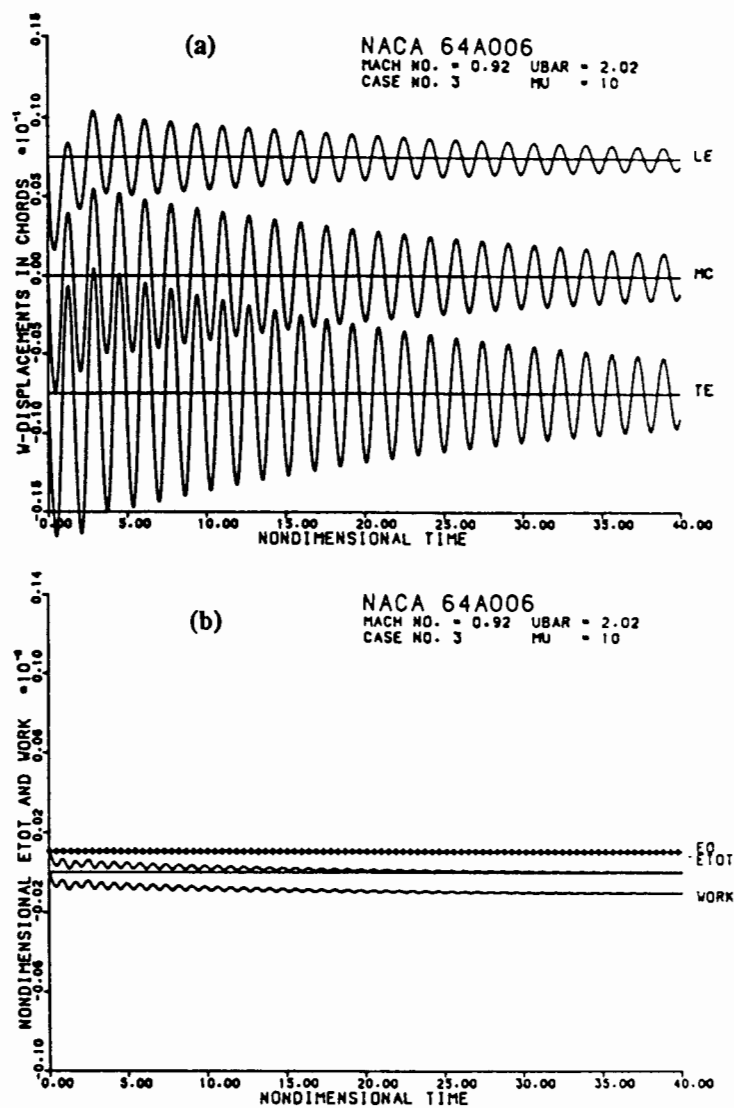
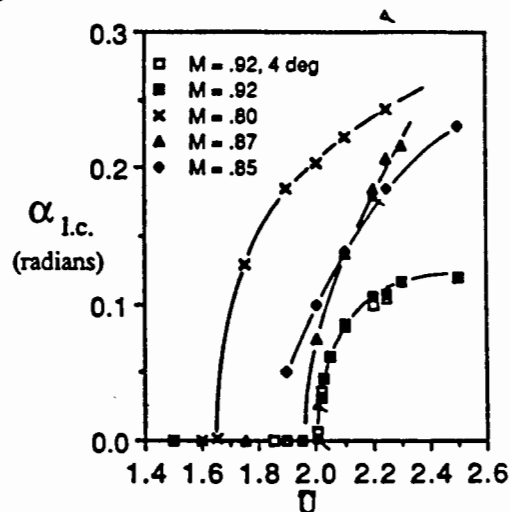Fig. 6 Stable aeroelastic response of NACA 64A006 wing for Case No. 3

Fig. 7 Bifurcation diagram for the NACA 64A006 wing model (Ref. 5), with present calculations indicated by flagged symbols
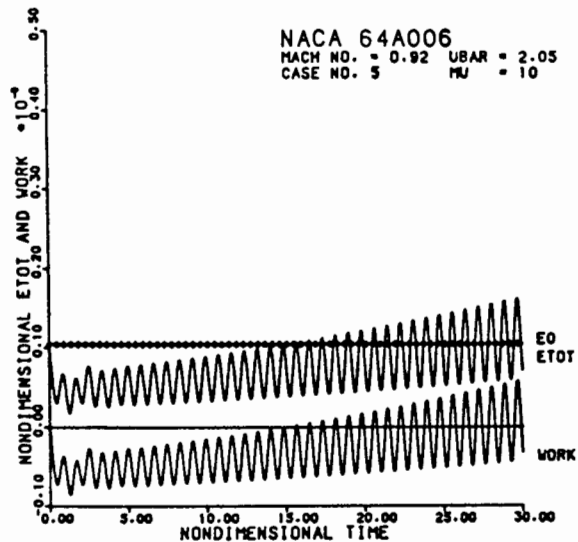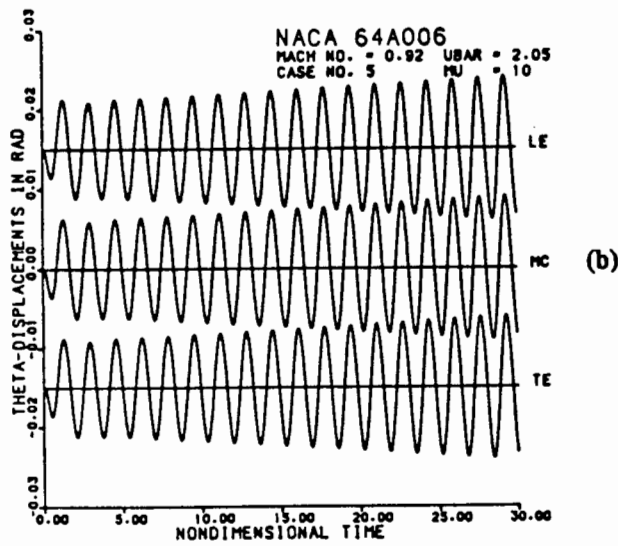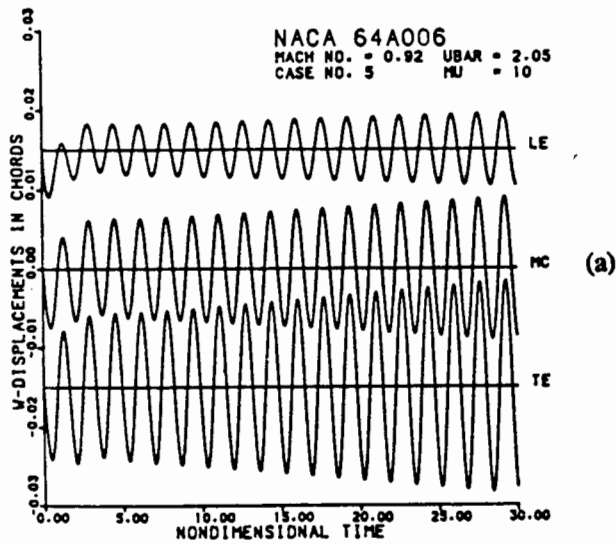
Fig. 8 Aeroelastic response of NACA 64A006 wing for Case No. 5, just past flutter boundary
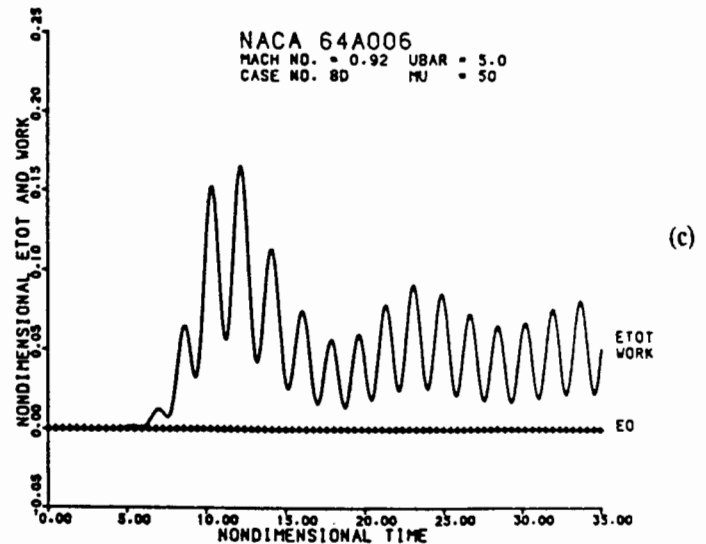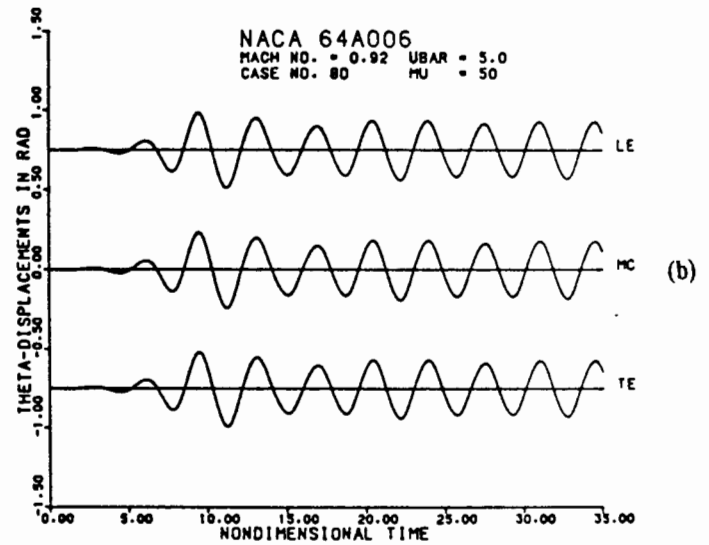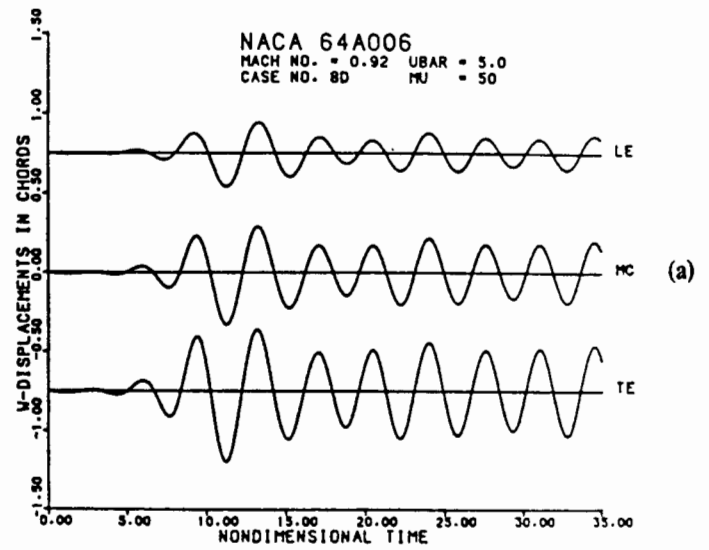
Fig. 9 Limit cycle flutter of NACA 64A006 wing, Case No. 8, calculated using five and eight finite elements
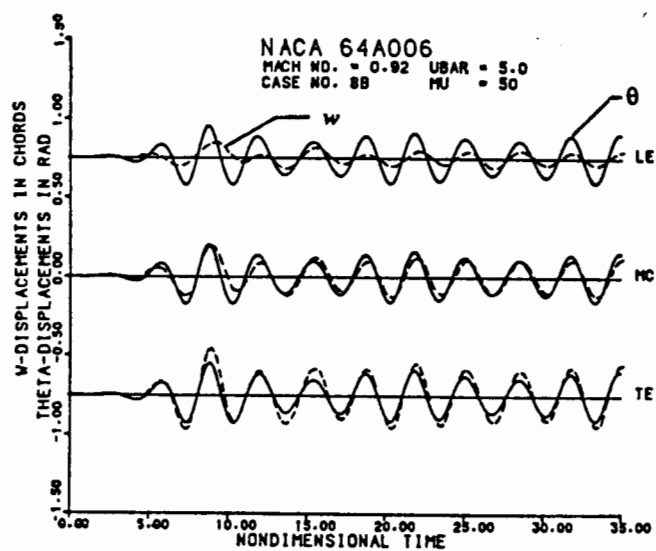
(a)
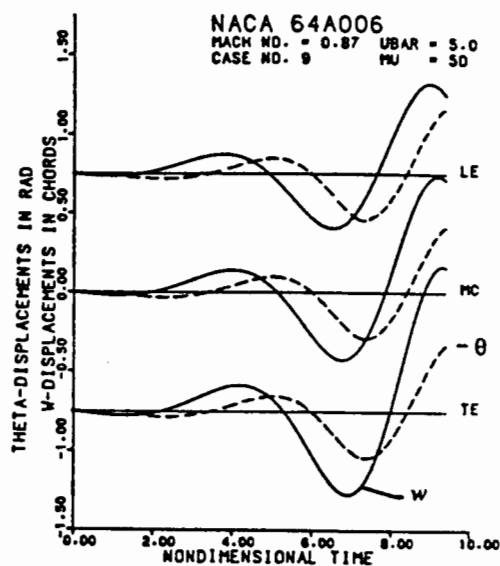
(a)
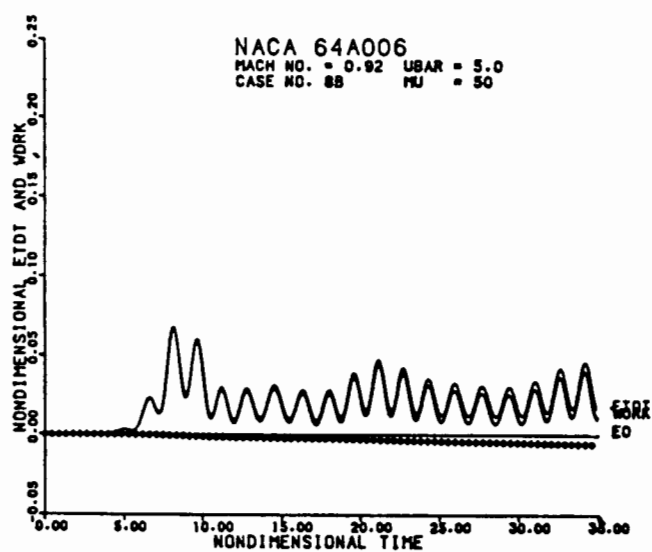
(b)
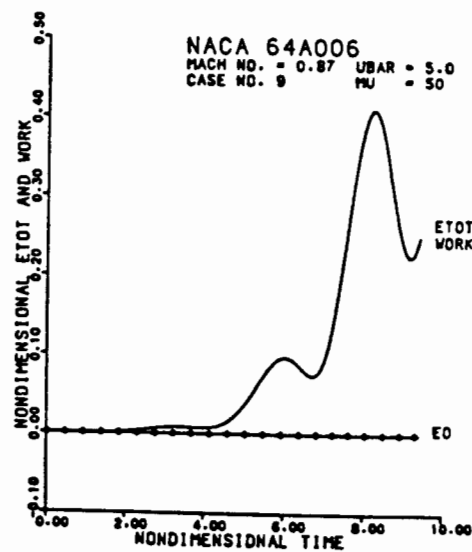
(b)

Fig. 10 Limit cycle flutter of NACA 64A006 wing,
Case No. 8, as calculated by the method of Ref. 5

Fig. 11 Explosive flutter of NACA 64A006 wing,
Case No. 9
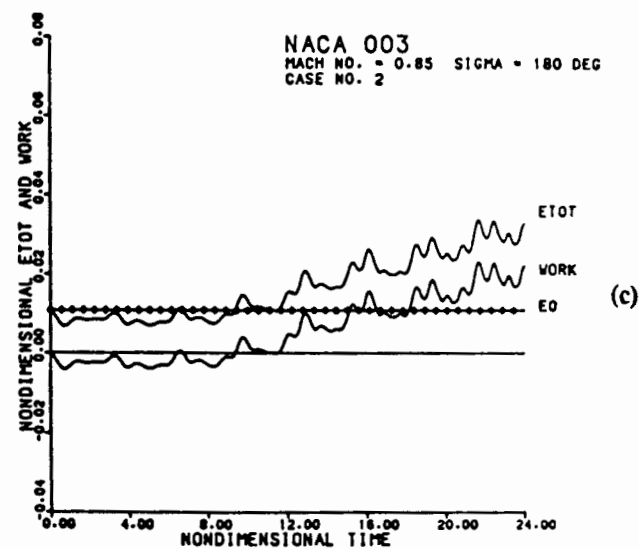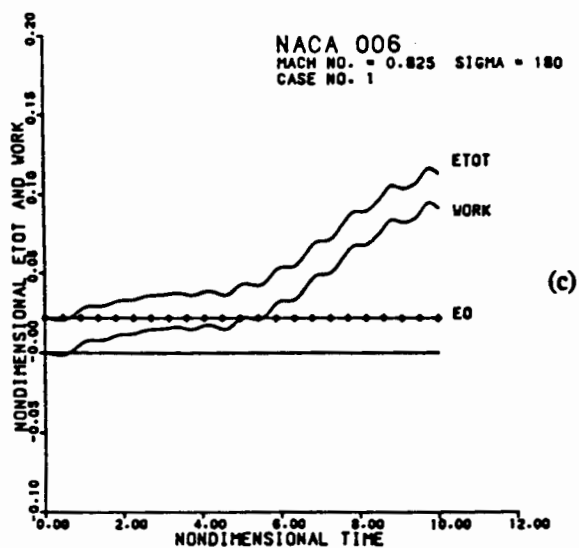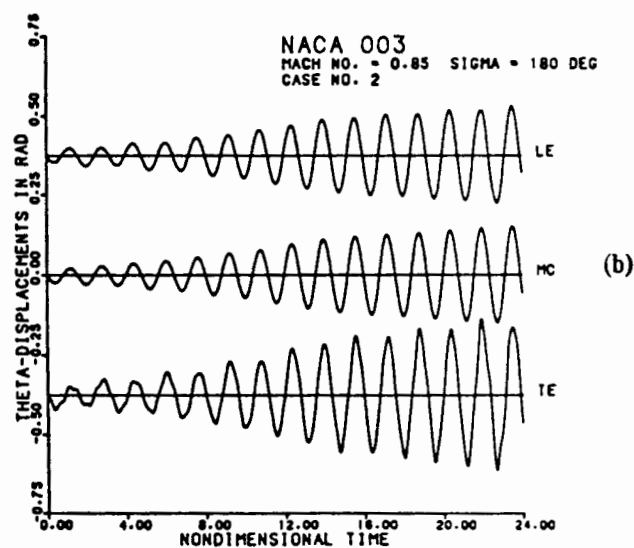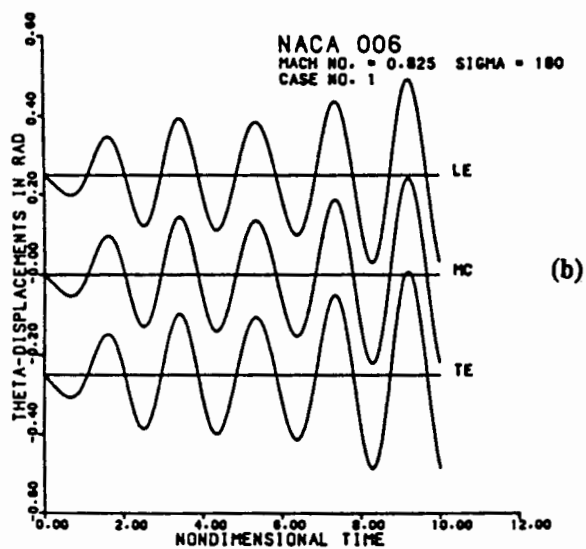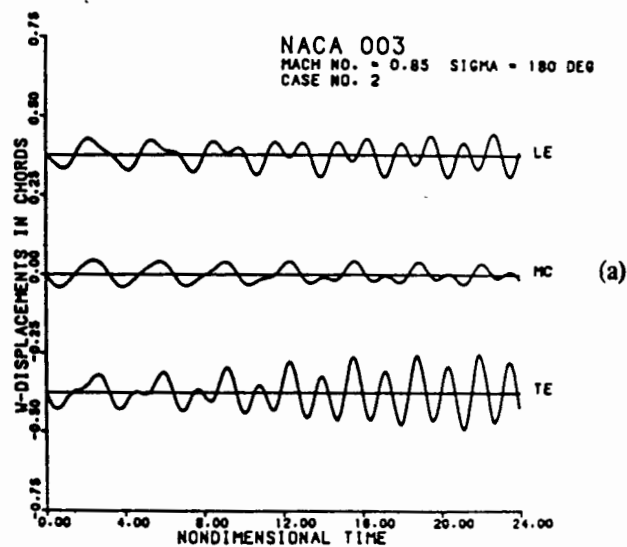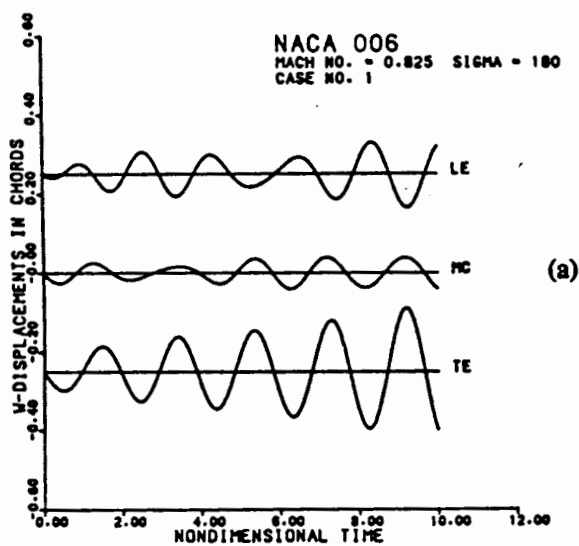
Fig. 12 Classical flutter behavior of NACA 006 cascade, Case No. 1

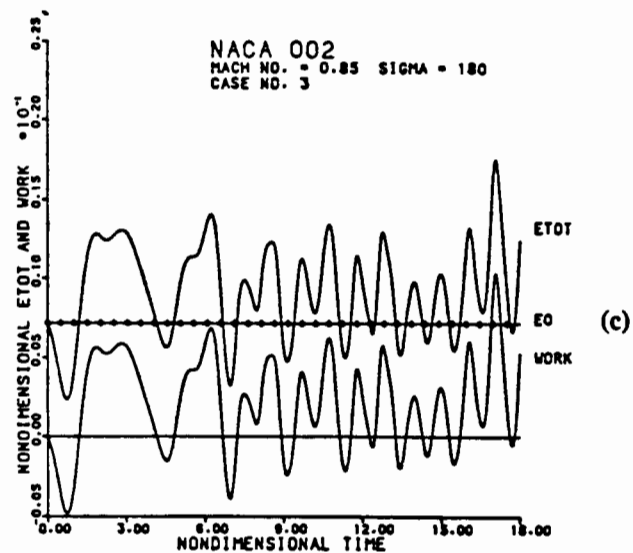Fig. 13 Aeroelastic response of NACA 003 cascade, Case No. 2. Flutter mode has significant chordwise bending
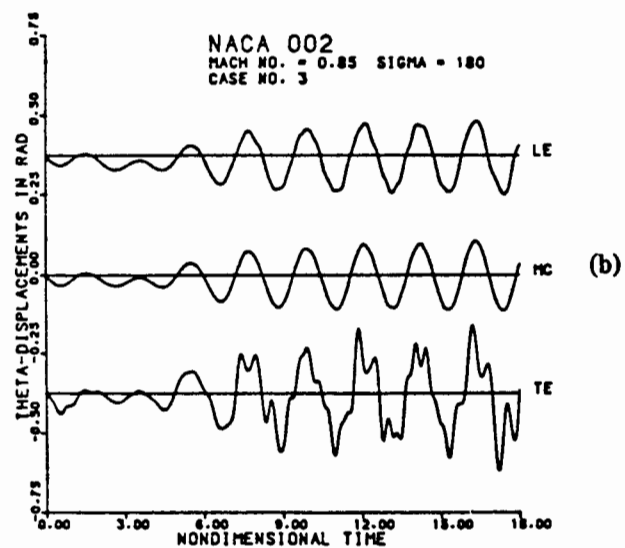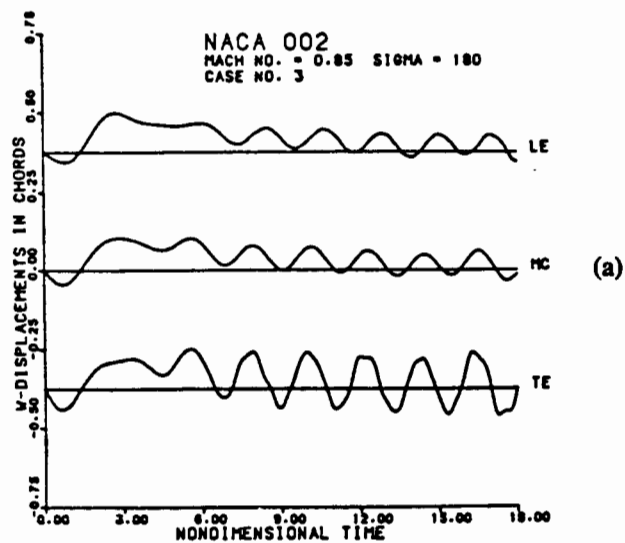
Fig. 14 Evidence of chordwise bending mode in flutter
time traces of NACA 002 cascade, Case No. 3